Geophys. J. Int. (1998) **132,** 584–594

A comparison of the Maslov integral seismogram and the finite-difference method

X. Huang,[1] J.-M. Kendall,[2] C. J. Thomson[3] and G. F. West[1]

[1] *Department of Physics, University of Toronto, Toronto, Ontario, Canada* M5S 1A7
[2] *Department of Earth Sciences, University of Leeds, Leeds,* LS2 9JT, *UK*
[3] *Department of Geological Sciences, Queen's University, Kingston, Ontario, Canada* K7L 3N6

Accepted 1997 September 2. Received 1997 August 4; in original form 1996 December 19

SUMMARY

The Maslov asymptotic method addresses some of the problems with standard ray theory, such as caustics and shadows. However, it has been applied relatively little, perhaps because its accuracy remains untested. In this study we examine Maslov integral (MI) seismograms by comparing them with finite-difference (FD) seismograms for several cases of interest, such as (1) velocity gradients generating traveltime triplications and shadows, (2) wave-front bending, kinking and folding in a low-velocity waveguide, and (3) wavefield propagation perturbed by a high-velocity slab.

The results show that many features of high- and intermediate-frequency waveforms are reliably predicted by Maslov's technique, but also that it is far less reliable and even fails for low frequencies. The terms 'high' and 'low' are model-dependent, but we mean the range over which it is sensible to discuss signals associated with identifiable wave fronts and local (if complicated) effects that potentially can be unravelled in interpretation. Of the high- and intermediate-frequency wave components, those wave-front anomalies due to wave-front bending, kinking, folding or rapid ray divergence can be accurately given by MI. True diffractions due to secondary wave-front sections are theoretically not included in Maslov theory (as they require true diffracted rays), but in practice they can often be satisfactorily predicted. This occurs roughly within a wavelength of the truncated geometrical wave front, where such diffractions are most important since their amplitudes may still be as large as half that on the geometrical wave front itself. Outside this region MI is inaccurate (although then the diffractions are usually small). Thus waveforms of high and intermediate frequencies are essentially controlled by classical wave-front geometry.

Our results also show that the accuracy of MI can be improved by rotating the Maslov integration axis so that the nearest wave-front anomaly is adequately 'sampled'. This rotation can be performed after ray tracing and it can serve to avoid pseudo-caustics by using it in conjunction with the phase-partitioning approach. The effort needed in phase partitioning has been reduced by using an interactive graphics technique.

It is difficult to formulate a general rule prescribing the limitations of MI accuracy because of model dependency. However, our experiences indicate that two space- and two timescales need to be considered. These are the pulse width in space, the length scale over which the instantaneous wave-front curvature changes, and the timescales of pulse width and significant features in the ray traveltime curve. It seems, from our examples, that when these scales are comparable, the Maslov method gives very acceptable results.

Key words: caustics, finite-difference methods, Maslov asymptotic theory, ray theory, seismic waveforms, shadows.

1 INTRODUCTION

Seismic waveforms are more sensitive to subsurface structures than are their traveltimes, so that waveforms can play an important role in controlled-source or earthquake seismic data interpretation. There are numerous approaches to modelling seismic waveforms, each having its own advantages and disadvantages, and with any technique there is always the question of accuracy and the practical problem of how to assess this accuracy (e.g. Weber 1988 for Gaussian beams). In this paper we explore the accuracy of Maslov asymptotic theory (Maslov 1965) through comparisons with finite-difference solutions. In an accompanying paper we introduce a new technique which extends the utility of the Maslov approach by combining it with the Kirchhoff method for complex waveform modelling (Huang, West & Kendall 1998).

Wave fronts and their amplitudes can be tracked through 3-D anisotropic media in a computationally quick fashion using geometric ray theory (GRT) (Červený 1972; Kendall & Thomson 1989). Unfortunately, GRT can break down in cases of special interest to seismologists (e.g. caustics). Maslov asymptotic theory is an extension of GRT which overcomes some of the limitations of ray theory while still preserving the flexibility and speed of ray tracing. The Maslov method was first introduced to seismology by Chapman & Drummond (1982) and since that time the theory has been adapted and developed by Thomson & Chapman (1986), Kendall & Thomson (1993), Brown (1994), Liu & Tromp (1996) and Huang & West (1997).

The Maslov method exploits the fact that rays form a 'Hamiltonian system' and so never cross in a 'phase space' comprised of the spatial (**x**) and slowness (**p**) coordinates. Phase space arises from considering not just instantaneous wave-front position, but also instantaneous speed and direction of propagation. It is 4-D for a 2-D earth model and 6-D for a 3-D model. In GRT we consider just rays and wavefields in the spatial domain (**x**), but these rays are in effect projected down from the higher-dimensional phase space to the spatial domain. Caustics result from singularities of this mapping, where rays cross in **x** and the GRT solution becomes infinite. (Maslov 1965; Maslov & Fedoriuk 1981) presented a uniform solution (i.e. valid everywhere) to the wave equation in a different way. He showed that the GRT singularities can be avoided by mapping the rays in phase space to a mixed subdomain [say for example (p_1, x_2, x_3) in a 3-D model] and that a spatial-domain wavefield is obtained via a type of Fourier transform between subdomains (e.g. from p_1 to x_1). The arguments are free-standing, geometrical and asymptotic, but they lead to already familiar results from separable solutions in laterally homogeneous media.

Maslov's approach avoids the ray-theory singularities associated with caustics, but it can create other singularities associated with the mapping to the mixed-space domain [pseudo-caustics (Klauder 1987), telescopic points (Frazer & Phinney 1980), y-domain caustics (Chapman & Drummond 1982), p-caustics (Brown 1994)]. Kendall & Thomson (1993) presented a technique, termed 'phase partitioning', which can be used to precondition the wave-front information in such a way that pseudo-caustics can be avoided. Following Arnold, Gusein-Zade & Varchenko's (1985) rules for a Lagrangian equivalence, the phase-partitioning method distorts the wave front in such a way as to preserve the Hamiltonian ray system. In Section 2 we review the Maslov integral, paying special attention to the phase-partitioning method.

Numerical finite differences (FD) (see Kelly & Marfurt 1990) provide some of the most general methods for solving the elastic wave equation. These techniques are extremely time-consuming or impractical in a computational sense, especially when treating 3-D anisotropic models and waveforms which are sharply resolved in time. A further disadvantage of FD methods is that they are not very well suited for data interpretation, especially where a trial-and-error approach to modelling is employed. By using ray-based techniques, one is afforded the luxury of being able to isolate specific phases and explore their sensitivity to model parameters in a relatively short amount of time. FD methods can be very accurate, and for this reason are ideally suited to testing the accuracy of other techniques; they have been employed in this study. In view of the computational times involved in the FD calculations we have restricted all our test models to 2-D cases.

Accuracy of the Maslov integral needs to be examined because Maslov's theory is only an asymptotic high-frequency approximation and observed seismic waves are frequency band-limited. In Section 3 we investigate the accuracy of Maslov integral seismograms by comparing them with FD seismograms for three interesting cases. These include: (1) velocity gradients generating traveltime triplications and shadows; (2) wave-front bending, kinking, and folding in a low-velocity waveguide; and (3) waveform propagation perturbed by a high-velocity slab. We also test the accuracy of the phase-partitioning technique and outline an interactive graphics method to reduce the effort needed in applying it.

2 THE MASLOV INTEGRAL SEISMOGRAM

Detailed formulations of Maslov asymptotic theory are given in Chapman & Drummond (1982) and Thomson & Chapman (1985) for isotropic elastic media and Kendall & Thomson (1993) for anisotropic media. This section reviews the theory briefly, highlighting salient points and terms required for implementation. For brevity the explanation here is restricted to acoustic media.

2.1 Maslov integral

In a 3-D acoustic medium, the frequency (ω) domain GRT solution for the Green's function G at a receiver point $\mathbf{x}_r = (x_{r1}, x_{r2}, x_{r3})$ is

$$G^{GRT}(\omega, \mathbf{x}_r) = \sum_{rays} \frac{\phi_0}{|\rho(\mathbf{x}_r) J(\mathbf{x}_r)|^{1/2}} \exp[-i\mathrm{sgn}(\omega)\pi\sigma/2] \times \exp[i\omega T(\mathbf{x}_r)], \quad (1)$$

where Σ sums all the rays arriving at $\mathbf{x}_r$ and the term ϕ_0 is the initial amplitude condition. The integer σ is the KMAH index, which monitors ray passage through caustics (Chapman & Drummond 1982). Normally the KMAH increases by unity, causing a $\pi/2$ phase shift in the waveform at every frequency. There are, though, less common cases where the ray passes through a point caustic (a focusing in three dimensions) and the KMAH increases by 2 (a phase shift of π). The amplitude of the arrival is controlled by the Jacobian of geometrical spreading J. In the ray coordinate system $\boldsymbol{\nu} = (T, q_1, q_2)$ of

initial take-off angles q_1 and q_2 and traveltime T, J is given by

$$J = \frac{\partial \mathbf{x}}{\partial \boldsymbol{\nu}} = \frac{\partial(x_1, x_2, x_3)}{\partial(T, q_1, q_2)} \tag{2}$$

(Červený 1972). At caustics, rays cross ($J \to 0$) and their amplitudes become infinite. There can also be shadow regions where no geometrical ray arrivals are predicted and yet diffracted signals are known to exist. Ray theory fails when a receiver is located in such places. The root of these problems is the dependence of ray theory on a single (or a few) infinitely narrow ray trajectory (Chapman & Drummond 1982).

Maslov theory, in contrast, constructs the wavefield as the sum of many neighbouring or 'non-geometrical' rays. This summation can be in one or two dimensions (Chapman & Drummond 1982), but for simplicity we illustrate the technique using 1-D summation. It is through this summation that the method can account for some lower-frequency effects. The Maslov formulation requires that a bundle of rays be traced from the source to a Maslov integration axis (MIA) (or plane in 2-D summation) along which lies the receiver point $\mathbf{x}_r$. The MIA can be arbitrarily rotated; for convenience it is usually arranged to be parallel to a coordinate axis such as the horizontal x_1-axis. Denoting the traced rays by their horizontal slownesses p_1, the traveltimes $T(p_1)$ and the ranges $x_1(p_1)$, the Maslov integral (MI) can be written

$$G^{\mathrm{MI}}(\omega, \mathbf{x}_r) = \left(\frac{i\omega}{2\pi}\right)^{1/2} \int \frac{\tilde{\phi}_0}{|\rho(p_1)\tilde{J}(p_1)|^{1/2}} \exp(-i\pi\tilde{\sigma}/2) \times \exp[i\omega\tilde{\theta}(x_{r1}, p_1)]dp_1, \tag{3}$$

where $\tilde{\phi}_0$ is the initial amplitude condition in the mixed or transform domain [(p_1, x_2, x_3) in our illustration]. The term $\tilde{\sigma}(p_1)$ is the Maslov index

$$\tilde{\sigma} = \sigma + [1 - \mathrm{sgn}(\partial x_1/\partial p_1)]/2. \tag{4}$$

By including the KMAH index σ, it ensures the continuity of the real waveform across a pseudo-caustic point (a place where rays focus in the transform domain) by increasing or decreasing its value by one whenever such a point is passed. More details can be found in Chapman & Drummond (1982), Garmany (1988), Kendall & Thomson (1993, Appendix A) and Brown (1994). The phase function $\tilde{\theta}(x_{r1}, p_1)$ is given by the intercept time τ and the Legendre transformation

$$\tilde{\theta}(x_{r1}, p_1) = \tau(p_1) + p_1 x_{r1}, \qquad \tau(p_1) = T(p_1) - p_1 x_1(p_1). \tag{5}$$

It can be thought of as the arrival time at x_{r1} of a 'plane wave' tangential to the physical wave front at the neighbouring point x_1 with slowness p_1 (Kendall & Thomson 1993, Fig. 1). Just as the GRT amplitude is inversely proportional to the square root of the ray-tube cross-sectional area in the real space, so the Maslov amplitude is inversely proportional to the square root of the transformed ray-tube cross-sectional area in the mixed domain. The geometrical spreading in the transform domain is controlled by the Maslov Jacobian $\tilde{J}$, related to the (GRT) Jacobian J through the 'canonical transformation'

$$\tilde{J} = J\frac{\partial p_1}{\partial x_1} = \frac{\partial(p_1, x_2, x_3)}{\partial(T, q_1, q_2)}. \tag{6}$$

The choice of MIA is not completely arbitrary. One tries to position the axis of integration to cross-cut the direction of most 'structure' in the wave front, as will be demonstrated later. By structure we mean folding, kinking or bending. It is numerically convenient to be able to calculate the Maslov Jacobian for the MIA rotated into the most appropriate direction *after* the rays are traced through the model at hand using the coordinates that are most natural. Rotating the MIA can often help mitigate problems with pseudo-caustics (see Huang 1997). For a rotated MIA, the Maslov Jacobian is given by

$$\tilde{J} = \mathbf{l}^{\mathrm{T}}\tilde{\mathbf{J}}\mathbf{l}, \tag{7}$$

where $\mathbf{l}$ denotes the directional vector of the MIA in the original coordinates and the matrix $\tilde{\mathbf{J}}$ is given by

$$\tilde{\mathbf{J}} = \{\tilde{j}_{mn}\}, \qquad \tilde{j}_{mn} = \frac{\partial \tilde{\mathbf{x}}_{mn}}{\partial \boldsymbol{\nu}}, \qquad m, n = 1, 2, 3. \tag{8}$$

In (8) we have introduced the symbol $\tilde{\mathbf{x}}_{mn}$ ($m, n = 1, 2, 3$) to denote any of nine mixed domains which are made up of two spatial coordinates and one slowness coordinate. For instance, $\tilde{\mathbf{x}}_{32} = (x_1, p_3, x_3)$, with x_2 replaced by p_3. The reader is referred to Huang (1997) for more details of the MIA rotation.

2.2 Maslov integral with phase partitioning

Pseudo-caustics occur in regions where there is ray focusing in the mixed domain [e.g. (p_1, x_2, x_3)]. In such cases the $\tilde{\theta}$-function and τ will show triplications, and the wave front in the spatial domain will be locally planar (that is the rays will be parallel) (Chapman & Drummond 1982; Kendall & Thomson 1993). The term 'pseudo' is used because they are a mathematical construct rather than a real physical wave-front feature. Unlike true caustics, pseudo-caustics will move when coordinate systems are changed (because they depend on the curvature of the coordinate lines/surfaces). At a pseudo-caustic the Maslov integral representation (3) breaks down because $\partial p_1/\partial x_1$ in eq. (6) becomes zero and the Maslov Jacobian vanishes (i.e. $\tilde{J} = 0$). To remedy this problem, Kendall & Thomson (1993) devised a phase-partitioning approach by involving the canonical property of a 'Lagrangian equivalence' (Arnold *et al.* 1985). This property ensures that a Lagrangian manifold (that is a hypersurface generated by rays in phase space) remains Hamiltonian in form even though its 'shape' in the new coordinate system differs from its original shape. The ultimate effects of such transformations can be to manipulate a Lagrangian manifold into a 'normal' form where no mapping singularities or 'catastrophes' arise because of projection from 6-D phase space to the mixed subdomain [e.g. (p_1, x_2, x_3)].

With phase partitioning a reference phase $T^{\mathrm{r}}(\mathbf{x})$ is selected in a way such that after subtracting it from the real phase, $T(\mathbf{x})$, the residual phase,

$$\bar{T}(\mathbf{x}) = T(\mathbf{x}) - T^{\mathrm{r}}(\mathbf{x}), \tag{9}$$

will be free of inflection points (i.e. locally plane sections) in the chosen coordinate system. Similarly, the relationship between the reference slowness $p_1^{\mathrm{r}}(\mathbf{x}) = \partial_{x_1} T^{\mathrm{r}}(\mathbf{x})$ and the residual slowness $\bar{p}_1(\mathbf{x}) = \partial_{x_1}\bar{T}(\mathbf{x})$ is

$$\bar{p}_1(\mathbf{x}) = p_1(\mathbf{x}) - p_1^{\mathrm{r}}(\mathbf{x}). \tag{10}$$

The result is that each ray is described by a unique residual slowness $\bar{p}_1(\mathbf{x})$. Finally, the residual curvature $\partial\bar{p}_1/\partial x_1$ is related to the reference curvature $\partial p_1^{\mathrm{r}}/\partial x_1$ by

$$\frac{\partial\bar{p}_1}{\partial x_1} = \frac{\partial p_1}{\partial x_1} - \frac{\partial p_1^{\mathrm{r}}}{\partial x_1}. \tag{11}$$

This ensures that the sign of the reference curvature along each branch of a traveltime triplication becomes constant (that is will never be zero; however it will still be infinite at real caustics). Implementation of the phase-partitioning method is further described in Kendall & Thomson (1993).

In terms of the new residual slowness the Maslov integral becomes (Kendall & Thomsen 1993)

$$G^{\mathrm{MI}}(\omega, \mathbf{x}_{\mathrm{r}}) = \left(\frac{i\omega}{2\pi}\right)^{1/2} \exp(i\omega T^{\mathrm{r}}(\mathbf{x}_{\mathrm{r}})) \int \frac{\bar{\phi}_0}{(\rho(\bar{p}_1)\bar{J}(\bar{p}_1))^{1/2}} \times \exp(-i\pi\bar{\sigma}/2) \exp[i\omega\bar{\theta}(x_{\mathrm{r}1}, \bar{p}_1)] d\bar{p}_1 , \quad (12)$$

where $\bar{\phi}_0$ is a constant. The Maslov index $\bar{\sigma}$ is obtained in a fashion similar to (4):

$$\bar{\sigma} = \sigma + [1 - \mathrm{sgn}(\partial x_1/\partial \bar{p}_1)]/2 . \quad (13)$$

The new phase function is simply

$$\bar{\theta}(x_{\mathrm{r}1}, \bar{p}_1) = \bar{\tau}(\bar{p}_1) + \bar{p}_1 x_{\mathrm{r}1}, \qquad \bar{\tau}(\bar{p}_1) = \bar{T}(\bar{p}_1) - \bar{p}_1 x_1(\bar{p}_1) . \quad (14)$$

The modified Maslov Jacobian becomes

$$\bar{J} = J\frac{\partial \bar{p}_1}{\partial x_1} = \frac{\partial(\bar{p}_1, x_2, x_3)}{\partial(T, q_1, q_2)} . \quad (15)$$

In Maslov's original work (Maslov 1965) pseudo-caustics were never considered a problem, partly because weighting functions were used to toggle between domains where GRT was valid and where MI was valid. Later, the work of Arnold on Lagrangian equivalences took it for granted that pseudo-caustics were absent (Arnold *et al.* 1985). However, seismological problems are generally frequency band-limited so that pseudo-caustics can occur near (within a wavelength of) real caustics and, furthermore, complicated non-linear coordinate changes are awkward to apply in practice. In such cases, phase partitioning is a better approach than using weighting functions. It should be noted that diffractions from caustics and end-point signals will move out with residual slownesses. This is significant when such signals persist far into diffraction regions, and they must then be corrected to obtain moveouts with the appropriate slownesses. This is described in detail in Huang (1997).

2.3 Numerical implementation

A Maslov waveform is a summation of rays in the neighbourhood of a receiver, and consequently the first step in the calculation is ray tracing. For the examples in this paper we use the ray tracer presented in Kendall & Thomson (1989) and its counterpart for 2-D acoustic media. The ray and geometrical-spreading equations are numerically integrated using a Runge–Kutta scheme. The models are specified on a regularly spaced grid and a quintic spline is used to interpolate continuous values and first and second derivatives of the medium parameters between the knot points (Huang 1997). The technique for performing the Maslov summation expressed in eqs (3) and (12) is discussed in Chapman, Chu & Lyness (1988). Appropriate modifications for 2-D media are given in Huang (1997). It is important to ensure that a sufficient density of rays are traced and included in the summation. The reader is referred to Chapman *et al.* (1988) and Guest & Kendall (1993) for more detail.

Numerical implementation of the phase partitioning requires an appropriate choice of reference phase. Kendall & Thomson (1993) suggested that the easiest way to implement phase partitioning was first to select a reference curvature which ensures that the wave front is free of inflection points by using interactive computer graphics. The reference slowness and phase are simply obtained from the reference curvature through successive integration. In our calculations the procedure consists of the following steps.

(1) Display the line of real curvature $\partial^2_{x_1} T(x_1)$ versus distance on the computer screen, the value of which is computed, for example from $\partial^2_{x_1} T = \tilde{J}/J$ (see eq. 6).

(2) Enter a set of master points such that their linear interpolation forms a piecewise straight line that does not intersect the real curvature. The line itself defines a function of the desired reference curvature. [Note that there are cases where this is not always possible; see Section 3.2 and Kendall & Thomson (1993).]

(3) Integrate piecewise the function of the reference curvature with respect to x_1, once giving the reference slowness and twice the reference phase. Both are analytically continuous.

Note that the reference phase obtained is second-order differentiable. The function of the reference curvature is not everywhere differentiable, but this should not cause any appreciable effect. The first example in the next section illustrates the technique. In addition, a situation is given in the second example where Step 2 does not fully apply.

3 TESTING THE ACCURACY OF THE MASLOV SOLUTION

This section presents comparisons of Maslov seismograms with finite-difference seismograms. In the first example 2-D FD elastic seismograms are calculated using a heterogeneous, explicit, fourth-order code developed by Clayton & Engquist (1977). The second and third examples show FD seismograms for the 2-D acoustic case calculated using a heterogeneous, explicit second-order code developed by Zeng (1996). Accuracy is ensured with sufficiently fine grid spacings and large model sizes. Both FD programs are equipped with first-order absorbing boundary conditions as presented in Clayton & Engquist (1977). The theoretical bases of these codes can be found in Clayton & Engquist (1977) and Zeng (1996). All calculations are performed on a SUN SPARCstation 10, where Maslov seismograms cost only tens of seconds of computation time, whereas FD seismograms cost tens of minutes.

3.1 Triplication and shadow

Sudden changes in velocity structure can cause wave-front folding, and hence traveltime triplications, which are commonly present in seismic observations. Here we model waveforms in the vicinity of a triplication using the Maslov method. The test model is 2-D elastic, with the *P*-wave velocity α, the *S*-wave velocity β and the density ρ varying only in the vertical direction (Fig. 1a). As simple as this model is, it produces interesting waveform effects.

Fig. 1(b) shows rays (and the corresponding wave fronts) propagating through this model from a point source at (0.21, 0.75). The rays in the fan from A to B give direct waves. They leave the source at an upward angle yielding a concave-upwards traveltime branch AB in Fig. 1(c). The rays from B to C are turning rays with a convex-downwards traveltime branch. The rays from C to D lie on the reversed branch of

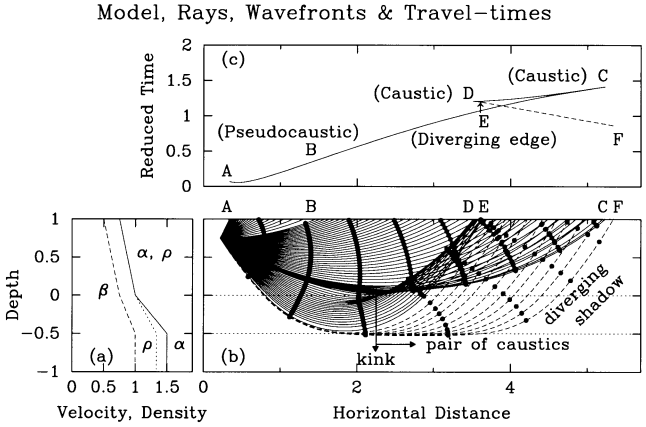

Figure 1. An isotropic model in which the elastic properties only vary with depth. (a) The velocity and density were discretized onto a grid and then interpolated using a quintic spline. Parameters are presented in dimensionless units. (b) The ray paths through the model (solid and dashed lines) and the corresponding wave fronts (dots). (c) The traveltime curve, reduced by $T = T_{\text{real}} - x_1/1.17$. The 'diffracted' branch EF is shown as a dashed line.

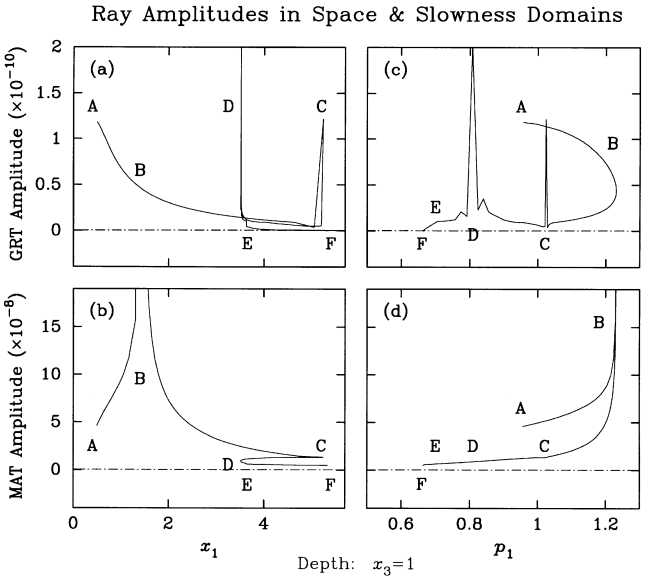

Figure 2. The GRT and Maslov amplitudes of the horizontal wavefield components. (a) GRT amplitude as a function of offset. (b) Maslov amplitude as a function of offset. (c) GRT amplitude as a function of slowness. (d) Maslov amplitude as a function of slowness. Both the GRT and Maslov amplitudes exhibit singularities (points C and D, and B, respectively) at different locations. These are marked by anomalously high amplitudes.

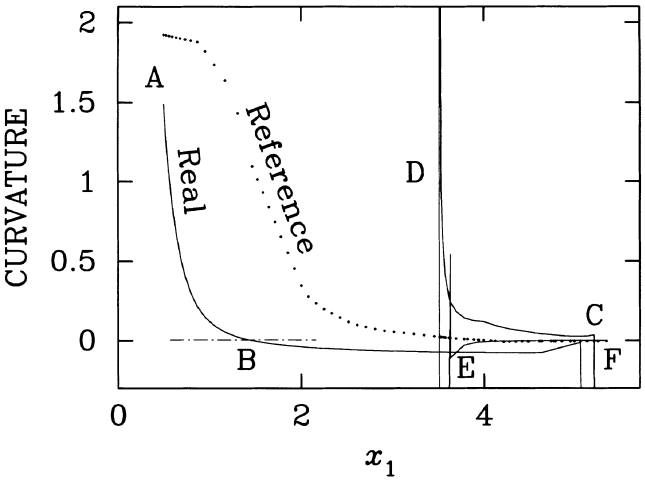

Figure 3. The first step in phase partitioning, which is used to remove the pseudo-caustic at B. The original phase curvature is shown as a solid line and a possible reference curvature is shown as a dotted line. The object is to find a reference curvature which will lie between the curvatures for each branch of the triplication.

the triplication and give rise to a concave-upwards traveltime branch. The rays from D to E are on the small second forward branch of the triplication and, like branch BC, form a convex-downwards branch. Point B corresponds to the ray which leaves the source horizontally and is the site of an inflection point ($\partial p_1/\partial x_1 = 0$) in the traveltime curve, thus marking the location of a pseudo-caustic. The pair of caustic surfaces which develop as the wavefront propagates intersect the receiver surface at points C and D, the cusps of the traveltime triplication. At the lowermost limit of the high-gradient part of the model (depth $= -0.5$) a suite of rays (shown as dashed lines in Fig. 1b) are drawn diverging from an infinitesimally small ray tube. The rays have vanishingly small amplitudes (Fig. 2) and the region they pass through is underilluminated. In this region, $\partial p_1/\partial x_1$ is very small because small changes in slowness, Δp_1, will produce large changes in offset, Δx_1. The suite could be called diffracted rays, since they arise in the smoothed model at the point where the original sharp gradient change existed and where, technically, the standard geometrical ray method would fail to model the wave effects correctly.

Fig. 2 shows the GRT and Maslov amplitudes of the horizontal components of the wavefield as functions of position and slowness. GRT is inaccurate near the caustics C and D, and in the underilluminated region beyond E where its amplitude is nearly zero. In contrast, the Maslov amplitude is finite everywhere except at the pseudo-caustic B (Figs 2b and d).

In order to calculate Maslov seismograms, we employ the phase-partitioning approach to remove the pseudo-caustic at B. Figs 3 and 4 illustrate the details of the procedure (see Kendall & Thomson 1993 for more detail). First, the real phase curvature is calculated (solid line in Fig. 3). For the downgoing rays, each branch of the triplication is of uniform sign in curvature as desired. The curvature changes sign at point B, the transition point from upgoing to downgoing rays. The curvature also switches sign between $+\infty$ and $-\infty$ at the caustics C and D (although not exactly because of discrete sampling). Note that the small spike near E is caused by the spline interpolation of the model. The next step is to choose a reference curvature which does not cross the original curvature along any of the branches (denoted by the dots at the ray arrivals in Fig. 3). This is carried out interactively on the computer screen. Note, though, that the reference curvature we use does cross the EF branch, but this does not cause a singularity in the Maslov integral because this branch shrinks to a point in the slowness domain (Fig. 2d).

The reference curvature is piecewise integrated with respect to x_1, once to produce the reference slowness and twice to produce the reference phase. Subtracting these reference values from the corresponding real functions gives the residual phase, residual slowness and residual curvature, shown in Figs 4(a),

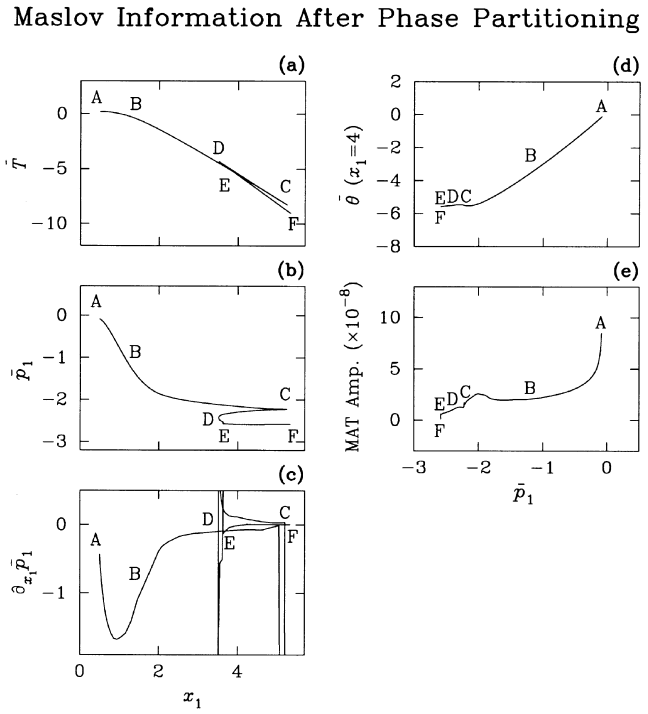

Figure 4. Intermediate information obtained from the reference curvature defined in Fig. 3. (a) The residual phase, now without an inflection point at B (compare with Fig. 1c). (b) The residual slowness. (c) The residual curvature. Note that this is now non-zero at point B. (d) The single-valued Maslov phase (at the position $x_1 = 4$) in the residual slowness domain. (e) The normalized Maslov amplitude in the residual slowness domain.

(b) and (c), respectively. Compared to the real phase (Fig. 1c), we see that the residual phase (Fig. 4a) no longer has an inflection point at B. Accordingly, the residual slowness no longer has a stationary point at B and the residual curvature is non-zero at B. In the residual slowness domain, the Maslov phase and amplitude, originally showing a triplication at the pseudo-caustic B, are now single-valued functions of the modified slowness in (d) and (e). Finally, the Maslov amplitude is no longer singular at point B.

Fig. 5 compares the waveforms of the horizontal components of the MI and FD wavefields for this model. The source signal for both is a band-limited, symmetric Gaussian wavelet. Fig. 5(a) shows that the MI and FD waveforms agree well not only for the simple geometrical signals, but also for the strongly interfering waves within the triplication. The enlargement shown in Fig. 5(b) reveals a relatively large difference between the caustic diffractions predicted by MI and FD beyond $x_1 = 6$, that is there is a degradation of MI in the deep shadow. Nevertheless, MI does a reasonable job of modelling the diffractions in this laterally homogeneous model, in the sense that they decay and deform with distance, and arrive at the correct times. Note that the separate branches of the traveltime curve in the triplicated area are not well resolved for this frequency range, and the geometrical arrivals merge with diffractions near the cusps C and D and with so-called diffracted rays beyond point E. Note that a weak *P–SV* converted wave from the $x_3 = 0$ gradient change is computed by FD. Fig. 5(c) shows there is also a good agreement between the amplitude spectra of these waveforms, where we can see

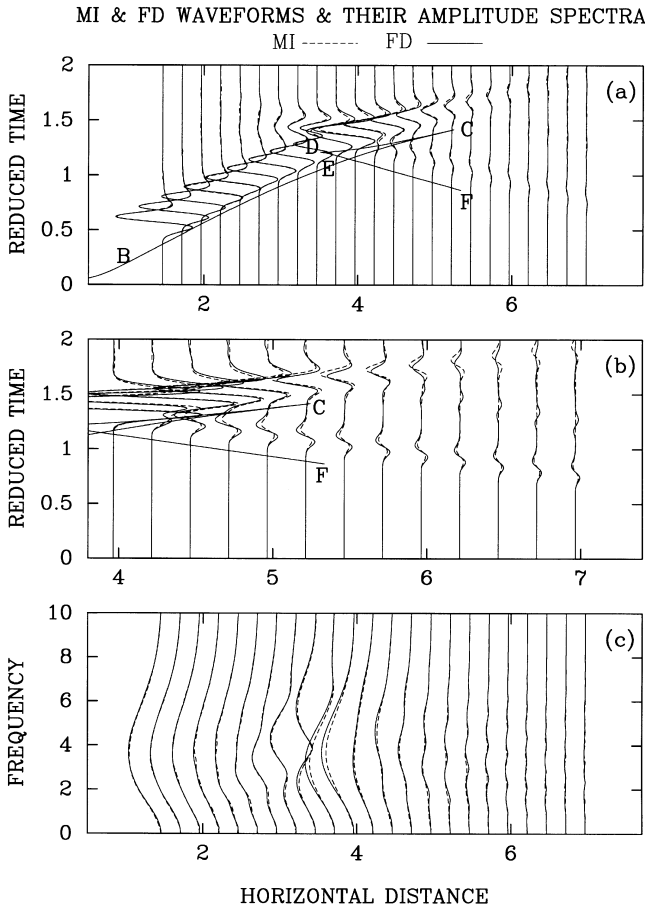

Figure 5. The 2-D horizontal MI (dashed) and FD (solid) waveforms for the model shown in Fig. 1. (b) Detail of the diffracted signals showing how MI slightly overestimates the cusp diffractions. Note that the weak arrivals which arrive just before the cusp diffractions and later than the EF-branch arrivals are converted *P–SV* waves generated only by the FD calculation at the upper first-order 'discontinuity' at a depth of 0 km. (c) The waveform amplitude spectra.

that the dominant dimensionless frequency is 3.6 units (that is 3.6 periods per unit of vertical traveltime to the first gradient change at $x_3 = 0$). There is a significant reduction of higher frequencies beyond the range $x_1 = 5$. The degradation of MI at low frequencies is illustrated in Fig. 6, where the dominant

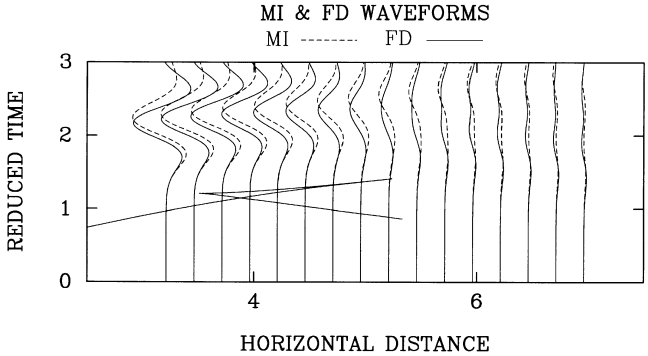

Figure 6. MI (dashed) and FD (solid) waveforms for the model shown in Fig. 1. These waveforms are much lower frequency than those shown in Fig. 5. Note that the Maslov waveforms no longer give a good fit with the FD waveforms. See text for details.

frequency has been reduced to 1 unit. At such a low frequency the wavefield is insensitive to the details of the structure.

3.2 Wavefront bending, kinking and folding

In this example we wish to examine waveform complexities before, during and after the development of a fold in a wave front. To do this we calculate waveforms at several stages as a wave front propagates horizontally through a horizontal low-velocity channel with a hyperbolic vertical velocity variation. Fig. 7 shows rays and wave fronts in this 2-D constant-density acoustic model of a waveguide. There are two types of cusp in the problem, those of the physical wave front and those of the caustic surface(s). The cusps on the folded wave front trace out two fold-caustic branches. The kink of the wave front exists where these two caustic branches themselves merge to form a *cusped caustic*. This is also known as a cusp catastrophe (Brown 1986) and in its vicinity the wavefield is mathematically described by the Pearcy function (Pearcy 1946). Note that the waveguide contains cascading series of caustics and pseudo-caustics.

Fig. 8 shows waveform snapshots obtained using Zeng's (1996) 2-D heterogeneous, explicit, second-order FD code equipped with Clayton & Engquist's (1977) first-order absorbing boundary conditions. An initially circular wavefront (a), grows in (b), bends at time (c), kinks at time (d), and then folds visibly at times (e) and thereafter. The wave front kinks again on the reversed branch in (h), eventually folding at time (i). Note that energy is concentrated at the bends, kinks, folds and cusps.

Maslov waveforms are calculated in the region around the first kink (Fig. 9). To include neighbouring rays, we simply integrate along a vertical axis. The phase-partitioning approach is again employed to remove the effects of pseudo-caustics. Fig. 9 shows the waveforms for the MI (dashed lines) and FD (solid lines) seismograms at the various locations marked by open circles in Fig. 7. Results are shown for the unfiltered case and a band-limited Gaussian wavelet. Note that the Maslov technique is less accurate in predicting the low-frequency waveform tails, but is very good at predicting the earlier parts of the waveform. In both modelling methods, the waveforms begin to be distorted before the fold, an effect geometric ray theory would not predict. Beyond this the waveform tails evolve into distinct geometrical and diffraction arrivals. All these features have been satisfactorily predicted by MI.

It should be noted that the phase-partitioning technique cannot be used to calculate waveforms in the region of the second kink and beyond. Just before the second kink at $x_1 = 2$, the reversed branch of the folded wave front develops two more pseudo-caustics. It is impossible to find a reference curvature which removes all of the pseudo-caustics in this region, thus we have no seismogram for this distance. Applying an alternate Lagrangian equivalance based on a change of the coordinate system is an interesting future possibility.

It is also interesting to compare the variations in Maslov waveforms with a choice of integration axes (MIAs). Fig. 10 shows the waveforms for three choices of MIA used at the receiver position (1.0, 0.24). The MI waveforms were created by integrating the rays to a MIA which passes to the left of the kink in (a), one which goes through the kink vertically (b) and one which passes through the fold (c). The resulting waveforms show that MI does a somewhat better job of predicting the distortion if the MIA passes vertically through the kink. This supports the view that the distortion is a diffraction effect which is essentially controlled by the geometry of the wave front, and that the integration should lie in the direction of maximum complexity in the wave front. Note that in this 2-D acoustic example, the diffracted tail has the same

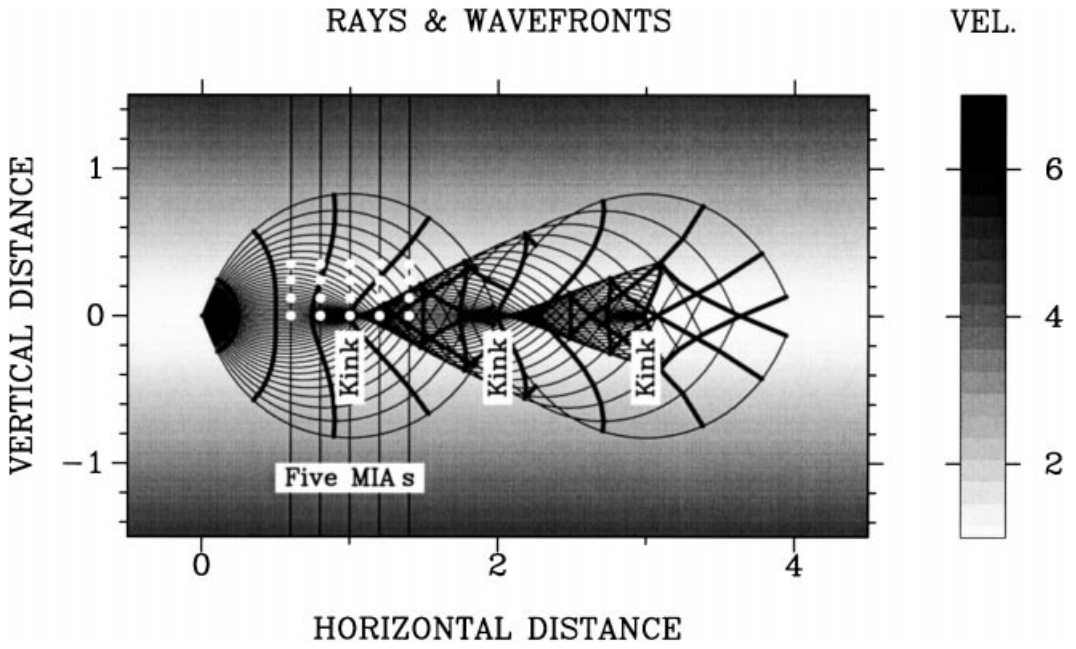

Figure 7. A 2-D acoustic waveguide in which the velocity (shaded in grey) increases hyperbolically away from the origin depth (zero). The rays (thin lines) emitted from the source are internally refracted, forming a series of caustics. The wave front (thick line) propagates initially as a circle, then bends, kinks and folds. Subsequent kinking and folding occurs on successive reversed branches of the folded wave front. The locations of five Maslov integration axes are indicated and open circles mark locations where Maslov waveforms are calculated.

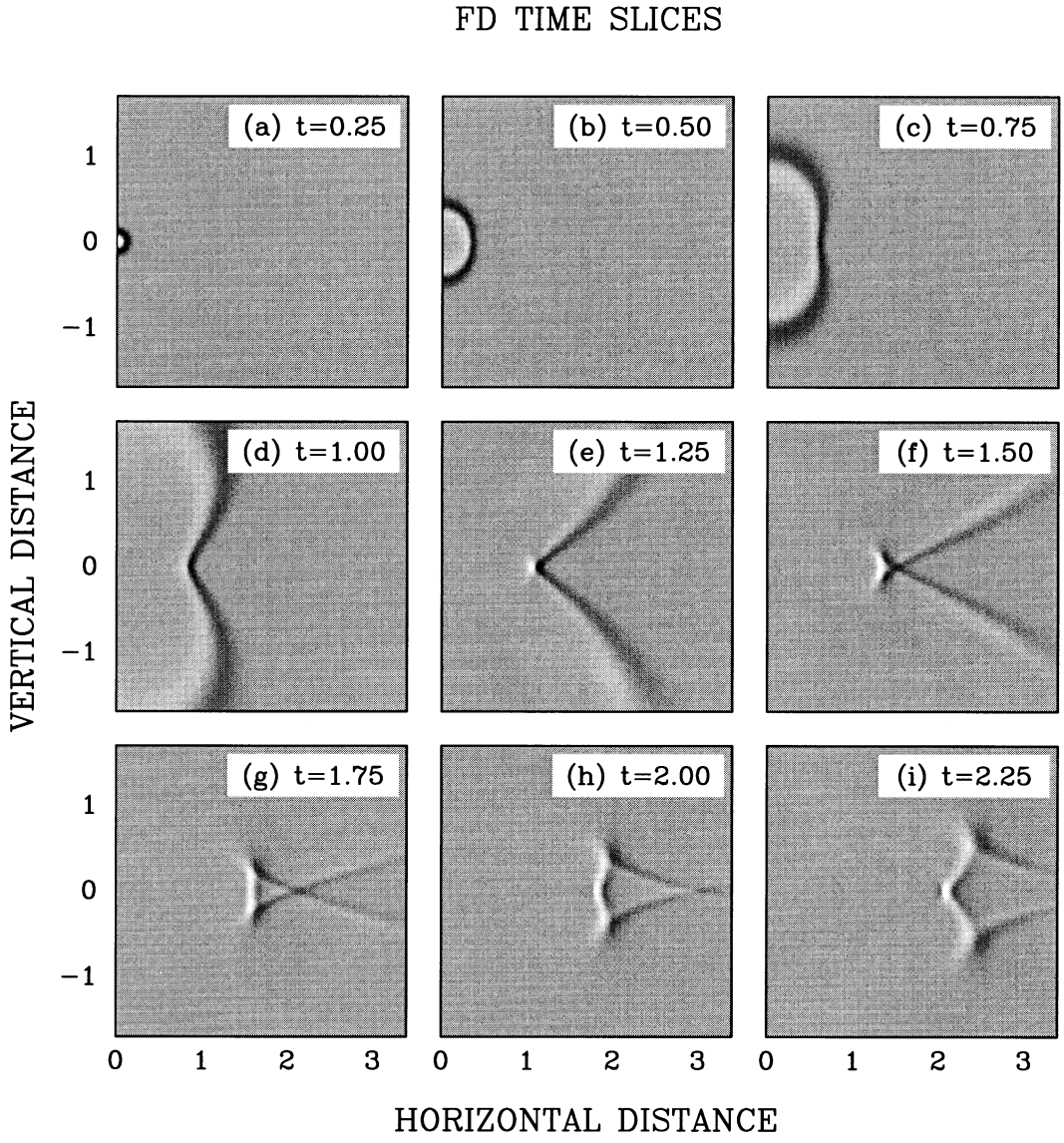

Figure 8. The FD time slices through the model shown in Fig. 7. (a) $t = 0.25$, a nearly circular wave front. (b) $t = 0.50$, an elliptic wave front. (c) $t = 0.75$, a bilobal wave front. (d) $t = 1.00$, a kink develops in the wave front. (e) $t = 1.25$, a small triplication emerges. (f) $t = 1.50$, the triplication gets bigger. (g) $t = 1.75$, the triplication develops inflection points on the reversed section. (h) $t = 2.00$, the triplication with the reversed branch kinked. (i) $t = 2.25$, another small triplication develops on the reversed branch of the original one.

sign as the primary impulse. This may not always be true. For vector waves, diffracted energy may sometimes make a waveform tail negative.

A point that should be noted is that because the wavefield near the kink changes rapidly, the number of sampling points per wavelength in the FD calculation must be high in order to avoid spurious grid dispersion. For the dominant frequency of 4 units and velocity of 1 unit used in the modelling, the wavelength is 0.25 units long and spans 43 grid points. This is roughly four times higher than the commonly used sampling rate or roughly 10 grid points per wavelength for second-order FD (Alford, Kelly & Boore 1974).

3.3 High-velocity slab

In this example we compare GRT, MI and FD waveforms for 2-D wave propagation through a high-velocity slab. The 2-D acoustic model (Fig. 11) has a constant background velocity of 1 unit and is perturbed by a Gaussian velocity anomaly which is 50 per cent higher in velocity at the centre of the slab than in the ambient model. The slab acts as an anti-waveguide to rays that propagate along the length of the high-velocity region. A smooth bend in the wave front develops just above the bottom of the slab (depth = 1 unit) where the faster and slower parts of the wave front meet. This smooth bend eventually becomes a kink and finally the wave front folds on either side of the slab. The triplication on the left half of the traveltime curve shown in Fig. 12 is the result of this folding. The effects of the triplication on GRT, MI and FD seismograms are compared for source-wavelet frequencies which are much lower than those which would resolve the three geometrical arrivals of the triplication and for a higher-frequency wavelet. The MI solutions were obtained using an observation line and MIA at a depth of 0.375 units and transverse to the slab. Note

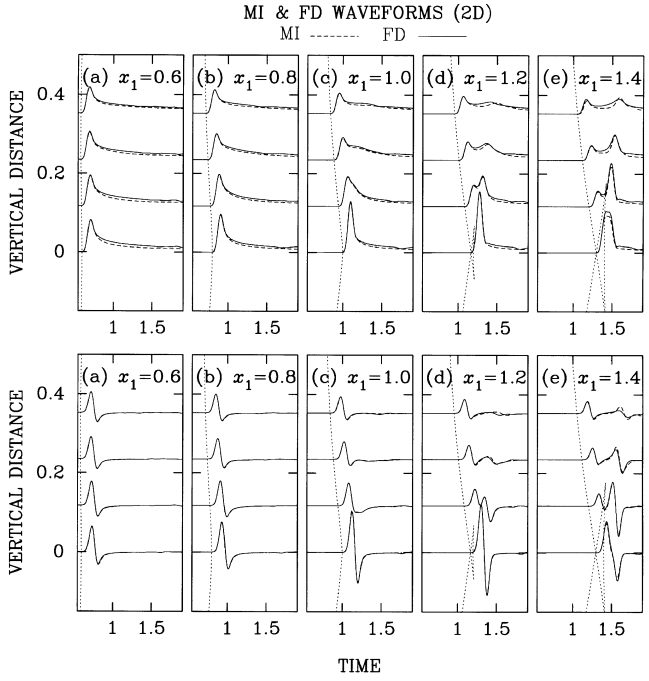

Figure 9. The MI (dashed) and FD (solid) waveforms as the wave front is (a) smooth; (b) bent; (c) kinked; (d) initially folded; and (e) folded. The dotted lines show the traveltimes. In the bottom figure the waveforms have been convolved with a band-limited Gaussian wavelet.

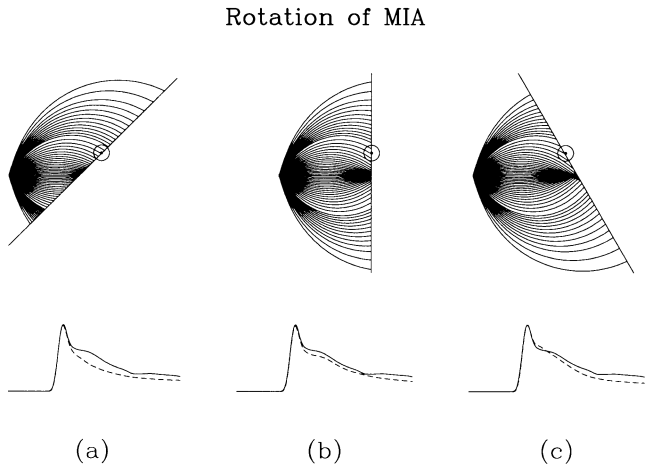

Figure 10. Maslov waveforms (dashed) generated using three rotated integration axes (MIAs) (as shown along the top). For comparison, the FD waveforms are shown as solid lines. The waveforms are calculated at the circled point (1.0, 0.24) just above the first kink in Fig. 7. The vertical MIA gives the most accurate result.

that more rays were actually used in their construction than are shown in Fig. 11.

Two pseudo-caustics arise in the neighbourhood of the triplication. This can be recognized by considering the curvatures of the traveltime curve in Fig. 12(a). The curve is concave upwards at the centre and far offset. On the reversed branch of the triplication the traveltime curve is also concave upwards. The curvature must change sign at the cusps, so as a cusp is approached along a forward branch, the curvature must change from concave to convex upwards (i.e. pass through zero). Phase partitioning has been used to remove the pseudo-caustics.

In Fig. 12, we show seismogram sections for the recording line in Fig. 11. Because the model is symmetrical in $x_1 = 0$, only half is shown. To save space a velocity reduction is applied on the timescale ($t = t + x_1/1.92$). Two cases are displayed: (a) using a high-frequency source wavelet and (b) using a low-frequency wavelet.

The wavelet in case (a) has a dominant period of about 0.025 units compared to the total traveltime of more than 2.5 units and a maximum triplication time difference of about 0.06 units. This is an ideal case for MI, and a good result is obtained. The strong forward branch of the traveltime curve A–B displays a normal wavelet; the strong reverse branch shows a Hilbert transform wavelet (time reverse in two dimensions), and the forward branch in the shadow zone shows a negligible amplitude. Diffractions are visible out from the cusps B and C, but they only extend for a Fresnel distance of order (wavelength × propagation distance)$^{1/2} \approx 0.2$ units (the dominant source wavelength is ~ 0.025 units; the path length from the wavefield bifurcation is ~ 1.5 units). GRT gives the correct waveform within each branch, but gives anomalously high amplitudes to the events at the cusps and zero amplitude to the diffractions, whereas MI is reasonably successful in these places.

The low-frequency case (b) is more revealing of MI error. First, we can easily calculate FD seismograms for this low-resolution case, and second, much greater strain is placed on the MI high-frequency asymptotic approximations. The dominant source wavelet period and wavelength are now ~ 0.5 units. This is about 1/6 of the total propagation path but five times the extent of the triplication, so the triplication is not resolved between B and C. There is still no amplitude in the shadow zone, but the diffractions from the two cusps are correspondingly more extensive [extending to $\sim (0.5 \times 1.5)^{1/2} \approx 0.9$ units of distance]. The group beyond B is relatively strong events that are diffracted by the left corner of the slab root. MI predicts all the direct events correctly and gives correct amplitudes and waveforms for most of the diffractions beyond B and C.

However, MI mispositions the diffractions into the deep shadows because of the phase partitioning used to eliminate pseudo-caustics. Note that the small, late arrivals across the upper-right corner are erroneous deep-shadow MI diffractions from the triplication on the right-hand side of the slab (that is the full spread of rays from left to right was used in the Maslov integration). This illustrates a weakness of the MI method. Although it often models diffractions in an appropriate fashion, one must be wary of the result. The ray manifold and traveltime curve contain no direct information about the propagation paths enountered by diffracted waves. The kinematics of any diffracted event are, at best, extrapolated from kinematic information contained in rays along nearby direct paths.

It is also interesting to note that when a wave propagates through a high-velocity slab, the wavefield along the slab is dominated at first by the direct events, then the distorted waveforms, and then the later diffractions.

4 CONCLUSIONS

Wave propagation in rapidly varying velocity structures will often produce caustics, shadows and waveform distortions.

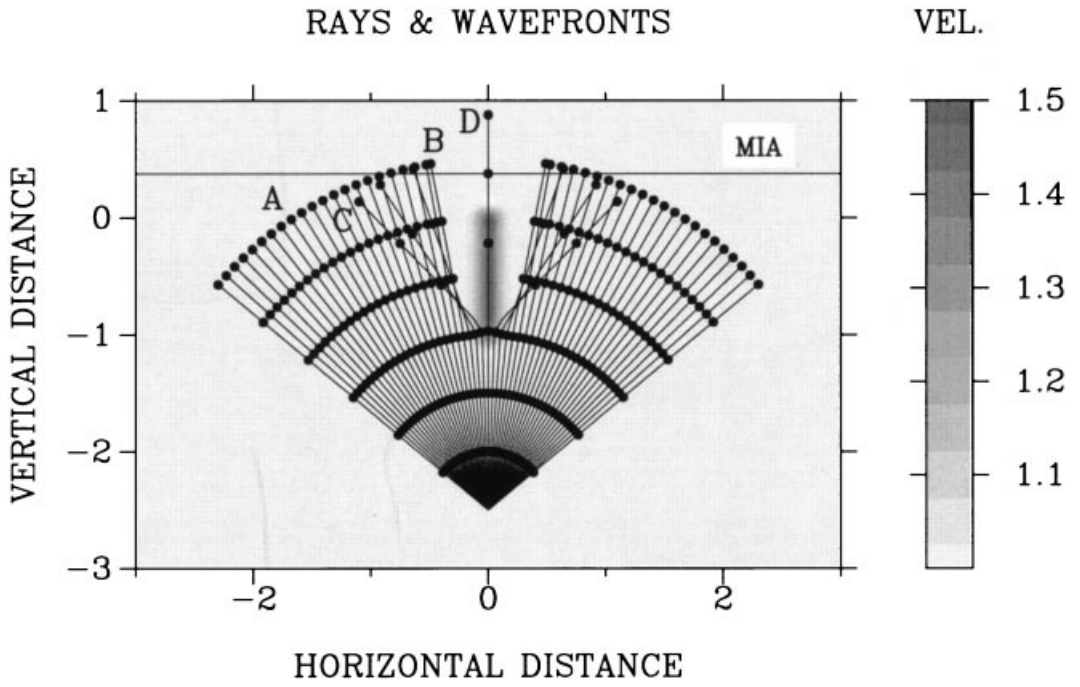

Figure 11. A 2-D acoustic high-velocity 'slab' model. The background is homogeneous with a velocity of 1 unit. The slab has a velocity perturbation up to 50 per cent described by the Gaussian $0.5e^{-(x_1/0.1)^2}$. The rays (lines) and wavefronts (dots) emanate from beneath the slab at point $(0, -2.5)$. The observation line (and Maslov integration axis) is shown at a vertical position of 0.375 units. Seismograms are calculated only for negative x_1, as the model is symmetric about $x_1 = 0$.

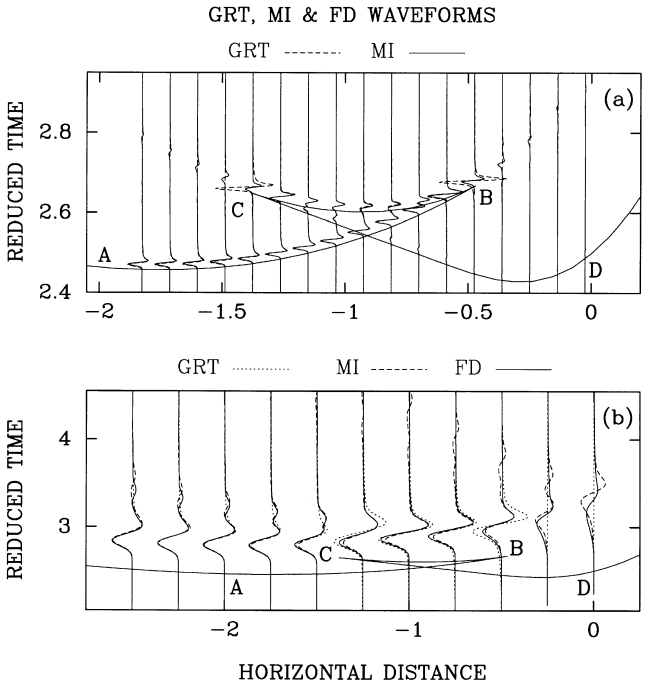

Figure 12. Waveforms of higher- (a) and lower- (b) frequency band source wavelets: (a) Comparison of MI (solid) and GRT (dashed) waveforms of higher-frequency band. (b) Comparison of MI (dashed), GRT (dotted) and FD (solid) waveforms of lower-frequency band. See text for more detail.

These distortions are informative because they are very sensitive to the Earth's heterogeneities. Unfortunately, in complex media simple geometrical ray theory cannot be used to predict these waveforms accurately. However, Maslov asymptotic theory, an extension of ray theory which retains the computational advantages, is expected to do a better job of modelling such effects.

We have tested the accuracy of the Maslov method for a number of cases by comparing the Maslov seismograms for finite-frequency source wavelets with those predicted using finite-difference methods. The results have shown that many important kinds of waveform distortion/diffraction can be efficiently and accurately predicted by the Maslov integral solution, provided the wave front is sufficiently well sampled and pseudo-caustics are removed. Maslov theory is inaccurate for very low-frequency signals, especially those deep inside shadow regions, which is to be expected because it is a high-frequency approximation. However, it appears that distorted waveforms of high/intermediate frequency can be accurately calculated from the wave-front information provided by ray tracing. Obviously, a general rule for prescribing the limitations of this accuracy is very difficult because of model dependency. However, our experiences indicate that two space- and two timescales need to be considered. These are the pulse width in space, the length scale over which the instantaneous wave-front curvature changes, and the timescales of pulse width and significant features in the ray traveltime curve. It seems, from our examples, that when these scales are comparable, the Maslov method gives very acceptable results.

Although our examination has been restricted to simple, continuous media, the results definitely apply to discontinuous and anisotropic environments (Guest & Kendall 1993). Furthermore, if a wave front contains rapid changes in three dimensions, then the 2-D Maslov integral solution should be used (Chapman & Drummond 1982; Kendall & Thomson 1993). Recent progress for this case has been made by Keers & Chapman (1995).

The connection between the Maslov technique and the Gaussian beam summation integral has been discussed by Klimeš (1984) and there are advantages and disadvantages with each approach. Infinitely wide beams lead to a summation which is equivalent to the Maslov method, but infinitely wide beams do not always work in complex media. This therefore leads to the problem of picking a beam width parameter in the Gaussian beam technique. It is not clear what happens to pseudo-caustics in the Gaussian beam method which treats beams in a complex space.

The phase-partitioning technique is quite simple to implement and works in many useful situations. Its drawbacks are (a) that it is in general not easily incorporated into an automated waveform modelling package and (b) that there are cases where phase partitioning breaks down altogether. In Section 3.2 it was shown that a low-velocity waveguide will quickly produce a situation where multiple caustics and pseudo-caustics are produced and phase partitioning cannot be used. An alternative and more easily automated technique for handling pseudo-caustics is presented in an accompanying paper by Huang *et al.* (1998).

ACKNOWLEDGMENTS

We thank Drs C. H. Chapman and T. Zhu for constructive discussions. We are also grateful to Dr X. Zeng for providing his FD codes. Constructive reviews by Michael Weber and an anonymous reviewer are gratefully appreciated. The research was supported by an E. F. Burton fellowship in the Department of Physics, University of Toronto, to XH, and NSERC funding to GFW, J-MK and CJT.

REFERENCES

Alford, R.M., Kelly, K.R. & Boore, D.M., 1974. Accuracy of finite-difference modeling of the acoustic wave equation, *Geophysics,* **39,** 834–842.

Arnold, V.I., Gusein-Zade, S.M. & Varchenko, A.N., 1985. *Singularities of Differentiable Maps,* Vol. 1, Birkhäuser, Boston, MA.

Brown, M.G., 1986. The transient wave fields in the vicinity of the cuspoid caustics, *J. acoust. Soc. Am.,* **79,** 1367–1384.

Brown, M.G., 1994. A Maslov–Chapman wavefield representation for wide-angle one-way propagation, *Geophys. J. Int.,* **116,** 513–526.

Červený, V., 1972. Seismic rays and ray intensities in inhomogeneous anisotropic media, *Geophys. J. R. astr. Soc.,* **29,** 1–13.

Chapman, C.H. & Drummond, R., 1982. Body-wave seismograms in inhomogeneous media using Maslov asymptotic theory, *Bull. seism. Soc. Am.,* **72,** S227–S317.

Chapman, C.H., Chu, J. & Lyness, D.G., 1988. The WKBJ seismogram algorithm, in *Seismological Algorithms,* pp. 47–74, ed. Doornbos, D.J., Academic Press, London.

Clayton, R.W. & Engquist, B., 1977. Absorbing boundary conditions for acoustic and elastic wave equations, *Bull. seism. Soc. Am.,* **67,** 1529–1540.

Frazer, L.N. & Phinney, R.A., 1980. The theory of finite frequency body wave synthetic seismograms in inhomogeneous elastic media, *Geophys. J. R. astr. Soc.,* **63,** 691–717.

Garmany, J., 1988. Seismograms in stratified anisotropic media–I. WKBJ theory, *Geophys. J.,* **92,** 365–377.

Guest, W.S. & Kendall, J.-M., 1993. Modelling seismic waveforms in anisotropic inhomogeneous media using ray and Maslov asymptotic theory: applications to exploration seismology, *Can. J. expl. Geophys.,* **29,** 78–92.

Huang, X., 1997. Contributions to seismogram modeling by classical Maslov and new Maslov–Kirchhoff methods, *PhD thesis,* University of Toronto, Canada.

Huang, X. & West, G.F., 1997. Effects of weighting functions on Maslov uniform seismograms: a robust weighting method, *Bull. seism. Soc. Am.,* **87,** 164–173.

Huang, X., West, G.F. & Kendall, J.-M., 1998. A Maslov–Kirchhoff seismogram method, *Geophys. J. Int.,* **132,** 595–602 (this issue).

Keers, H. & Chapman, C.H., 1995. 2D Maslov integrals and pseudo-caustics, *EOS, Trans. Am. geophys. Un.,* F370.

Kelly, K.R. & Marfurt, K.J., 1990. *Numerical Modeling of Seismic Wave Propagation,* Soc. Expl. Geophys., Tulsa, OK.

Kendall, J.-M. & Thomson, C.J., 1989. A comment on the form of the geometrical spreading equations, with some numerical examples of seismic ray tracing in inhomogeneous, anisotropic media, *Geophys. J. Int.,* **99,** 401–413.

Kendall, J.-M. & Thomson, C.J., 1993. Maslov ray summation, pseudo-caustics, Lagrangian equivalence and transient seismic waveforms, *Geophys. J. Int.,* **113,** 186–214.

Klauder, J.R., 1987. Global, uniform, asymptotic wave-equation solutions for large wavenumbers, *Ann. Phys.,* **180,** 108–151.

Klimeš, L., 1984. The relation between Gaussian beams and Maslov asymptotic theory, *Studia Geophy. Geod.,* **28,** 237–247.

Liu, X. & Tromp, J., 1996. Uniformly valid body-wave ray theory, *Geophys. J. Int.,* **127,** 461–491.

Maslov, V.P., 1965. *Theory of Perturbations and Asymptotic Methods* Izd., MGU, Moscow (in Russian).

Maslov, V.P. & Fedoriuk, M.V., 1981. *Semi-Classical Approximation in Quantum Mechanics,* D. Reidel, Dordrecht, the Netherlands.

Pearcy, T., 1946. The structure of an electromagnetic field in the neighborhood of a cusp of a caustic, *Phil. Mag.,* **37,** 311–317.

Thomson, C.J. & Chapman, C.H., 1985. An introduction to Maslov's asymptotic method, *Geophys. J. R. astr. Soc.,* **83,** 143–168.

Thomson, C.J. & Chapman, C.H., 1986. End-point contributions to synthetic seismograms, *Geophys. J. R. astr. Soc.,* **87,** 285–294.

Weber, M., 1988. Computation of body-wave seismograms in absorbing 2-D media using the Guassian beam method: comparison with exact methods, *Geophys. J. R. astr. Soc.,* **92,** 9–24.

Zeng, X., 1996. Finite difference modeling of viscoelastic wave propagation in a generally heterogeneous medium in the time domain, and a dissection method in the frequency domain, *PhD thesis,* University of Toronto, Canada.